Bactericidal and bioinspired chitin-based anisotropic layer-by-layer brushed-nanocoating

Muhammad Haseeb Iqbal, Fabienne Quilès, Emeline Pradel, Sarah Benmalek-Kehili, Christine Lancelon-Pin, Laurent Heux, Florent Meyer, Lydie Ploux, Gregory Francius, Fouzia Boulmedais

Bactericidal and Bioinspired Chitin-Based Anisotropic Layer-by-Layer Brushed-Nanocoating

Muhammad Haseeb Iqbal [a], Fabienne Quilès[b], Emeline Pradel [a], Sarah Benmalek-Kehili [a], Christine Lancelon-Pin [c], Laurent Heux[c], Florent Meyer[d,e], Lydie Ploux[d,e], Grégory Francius[b], and Fouzia Boulmedais* [a]

a. Université de Strasbourg, CNRS, Institut Charles Sadron, UPR 22, Strasbourg, 67034, France

b. Université de Lorraine, CNRS, LCPME, F-54000 Nancy, France

c. Université Grenoble Alpes, CNRS, CERMAV, Grenoble, 38041, France

d. Centre de Recherche en Biomédecine de Strasbourg, Institut National de la Santé et de la Recherche Médicale, UMR 1121, Biomatériaux et Bioingénierie, Strasbourg Cedex, 67085, France

e. Université de Strasbourg, Faculté de Chirurgie Dentaire, Strasbourg, 67000, France

***Corresponding authors.** E-mail: fouzia.boulmedais@ics-cnrs.unistra.fr

Tel: +33 03 88 41 41 60

Abstract

Top-down biomimetic surfaces with micro/nanotopographic features have emerged as a strategy to prevent bacterial attachment and biofilm formation. These nanostructured surfaces mimic the nano-micro topographical features found naturally on cicada wings. However, their development requires expensive equipment and complex processes. Here, inspired by butterfly wings and crustacean exoskeletons, we present the simple design of fully bio-based, anisotropic, and antibacterial layer-by-layer (LbL) coatings based on chitin nanocrystals (ChNCs). Composed exclusively of US Food and Drug Administration-approved materials, the LbL nanocoatings were obtained by manual brushing of ChNC and Tannic Acid (TA), a natural polyphenol, coordinated by iron III (Fe^{3+}). In contrast to those obtained by the dipping method, the brushed TA/Fe^{3+}/ChNC coatings exhibit highly oriented ChNC nanostructures that enable contact-killing antibacterial properties against *Staphylococcus aureus* (a Gram-positive bacterium) and *Escherichia coli* (a Gram-negative bacterium). This antibacterial property is due to the orientation of the ChNC into spike-like nanotopographies with a high density of positive charge on the surface. Similar to cicada and dragonfly wings, the positively charged spikes of the oriented ChNC films are likely to damage the bacterial cell wall by (i) puncturing it upon contact with the spikes and/or (ii) stretching and tearing it when a shear force detaches the cell from the highly positive surface. The fully bio-based nature of ChNC-based nanocoatings and their brush-based fabrication method make them a suitable and affordable candidate as a sustainable antibacterial film for (bio)materials in biomedical and environmental applications.

Keywords: Orientation, multilayers, bio-sourced, nanotopography, nanostructured surfaces, antibacterial

Introduction

Nanostructured surface coatings have attracted great attention in the last decade to develop advanced next-generation materials. Antibacterial surface modification is of paramount importance to address bacterial infections, a major threat to human health worldwide. Antibacterial coatings are developed either by top-down *i.e.*, physicomechanical structuring of surfaces,[1] or bottom-up approaches that typically involve chemical modification of surfaces.[2] Top-down biomimetic surfaces with micro/nano-topographical features have emerged as a strategy to prevent bacterial attachment and biofilm formation.[3] These nanostructured surfaces are inspired by the nano-micro-topographic features found naturally on cicada wings,[3] lotus leaves, gecko feet, and shark skin.[4] However, their development requires expensive equipment and complex processes such as laser ablation,[1] electropolishing, and photolithographic techniques.[4, 5]

The chemical modification includes surface functionalization with antimicrobial peptides,[6, 7] silver nanoparticles, antibiotics, and synthetic or bio-based polymers.[8] Among the numerous bottom-up surface functionalization strategies, the layer-by-layer (LbL) method is one of the simplest and most versatile techniques, based on the alternate deposition of positively and negatively charged polyelectrolytes on a substrate via dipping,[9] spin coating,[10] or spray assembly.[11] Because of its ease of application to almost any substrate shape and size, and its mild preparation conditions (aqueous solutions, room temperature), it has been widely used to develop anti-adhesive or bacteriostatic, contact-killing, and release-killing antimicrobial surfaces.[12] Recently, a brush-based LbL method has been introduced using paint brushes, synthetic polyelectrolytes, and soluble polysaccharides.[13] The shear effect of the brushing technique has been reported to align the monolayer of clay nanotubes,[14] hydroxyapatite micro- to nano-fibers,[15] and collagen to develop human muscle fibers *in-vitro*.[16]

Extracted by acid hydrolysis from crustacean exoskeletons,[17] highly anisotropic crystalline chitin nanocrystals and nanofibers are commonly used for their excellent mechanical properties to design biodegradable three-dimensional (3D) materials[18] or films.[19] Using expensive types of

equipment, chitin-based oriented nanostructures have been designed using electric[20] and magnetic fields,[21] shear,[22] and wet stretching[23] to develop optically anisotropic or mechanically robust films. However, despite the well-known antibacterial properties of chitosan,[24] a deacetylated compound of chitin, few studies have reported chitin-based membranes or 3D materials with antifungal [25] or antibacterial properties.[26, 27] Fungal and bacterial inhibitions have rarely been achieved with pristine chitin,[25] but mostly with chemically modified chitin,[27] or by incorporating chitosan[26] or other antipathogenic agents such as copper.[28] Furthermore, none of the few studies on chitin-based LbL obtained by the dipping method,[29-32] reported antibacterial properties of the bio-sourced film.

Here, inspired by chitin-based butterfly wings[33] and iron-rich crustacean exoskeletons,[34] we report the simple design of fully bio-sourced, anisotropic, and antibacterial LbL coatings based on chitin nanocrystals (ChNCs) using the brushing method (Figure 1 and Supporting Information Figure S1). Composed exclusively of FDA-approved materials (FDA: United States Food and Drug Administration),[35, 36] the LbL nanocoatings were obtained by manual brushing of ChNC and tannic acid (TA), an abundant natural polyphenol with intermediate dipping in an iron III (Fe^{3+}) solution to ensure coordination bonding with both TA and ChNC.[37]

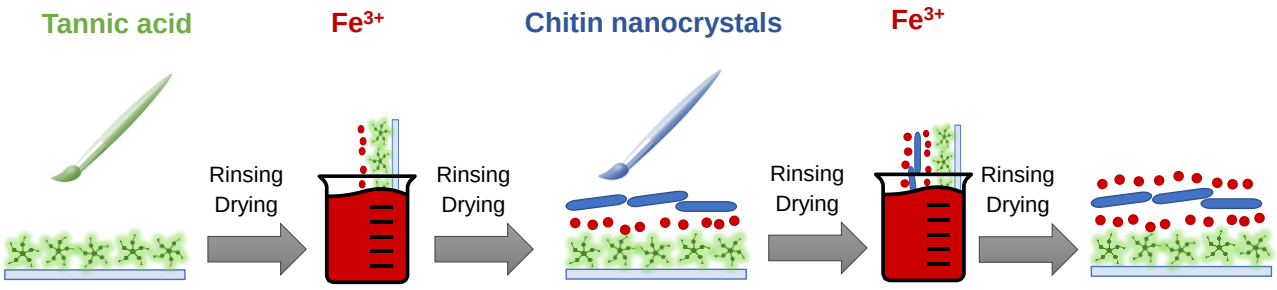

Figure 1: The LbL brushing method. Schematic representation of anisotropic ChNC film's buildup by the brushing LbL method based on the cycling deposition of (TA/Fe^{3+}/ChNC/Fe^{3+}). After the deposition of TA or ChNC by the paintbrush, an adlayer of Fe^{3+} is deposited by dipping alternated by the rinsing step with ultrapure water and the drying step by compressed air along the brushing direction. Paintbrush image from stockio.com for commercial use.

In contrast to those obtained by the dipping method, the brushed TA/Fe^{3+}/ChNC coatings exhibit highly oriented ChNC nanostructures, which enable contact-killing antibacterial properties against *Staphylococcus aureus* (*S. aureus*, a Gram-positive bacterium) and *Escherichia coli* (*E. coli*, a Gram-negative bacterium). The main focus of this study is on a comprehensive evaluation of the physicochemical and antibacterial properties of brushed and dipped TA/Fe^{3+}/ChNC/Fe^{3+} coatings to decipher their mechanism of action.

1. Results and discussion

1.1. The brushing method aligns chitin nanocrystals in LbL films

Anisotropic elongated nanostructured ChNCs suspension was obtained from chitin powder using a previously described protocol.[17] The ChNC nanostructure size was measured at 116 nm by dynamic light scattering measurements and confirmed by atomic force microscopy (AFM) with 116 ± 8 nm in length and 10 ± 2 nm in width (Supporting Information Figure S2). They showed strong cationic character with a zeta potential of +48.3 mV due to the presence of protonation of some amino groups that have been formed by deacetylation of surface N-acetyl amido groups.[18] Since the ChNC suspension was at pH 3 to ensure its long-term stability during storage, all the LbL buildups were performed with all solutions prepared at pH ≤ 3. Based on chitosan/TA[38] and chitosan/Fe^{3+}[39] interactions, ChNC/Fe^{3+} and ChNC/TA LbL films were built up on a poly(ethylene imine) (PEI) precursor layer by manual brushing, which showed limited thickness growth (Supporting Information Figure S3-S4**)**. Thus, the deposition of (TA/Fe^{3+}/ChNC/Fe^{3+}) quadrilayers was enabled by the coordination bonds known to allow TA to interact with Fe^{3+},[37] resulting in the so-called brushed ChNC films. The dipping method was used for a control surface, which was named dipped ChNC films. The thickness of the brushed ChNC film increases linearly as a function of the last deposition step reaching up to 24.8 ± 0.8 nm after 8 quadrilayers, *i.e.* PEI-(TA/Fe^{3+}/ChNC/Fe^{3+})$_8$. In contrast, irregular growth of the dipped films was obtained reaching a plateau of 121.3 ± 2.8 nm after 7 quadrilayers (Figure 2a). The main thickness increase comes from ChNC (about 15-20 nm corresponding to 1-2 ChNC thick). The reduced amount of suspension and the high shear effect of

the brushing method lead to a smaller thickness increment of ChNC compared to the dipping method as reported for other systems.[13] The small increment may also result from the different refractive index values in a direction parallel or perpendicular to their long axis[40] which can explain the small thickness increment of ChNC. The dipped and brushed ChNC/TA films were stable in PBS with no significant loss of dry thickness (Figure 2a).

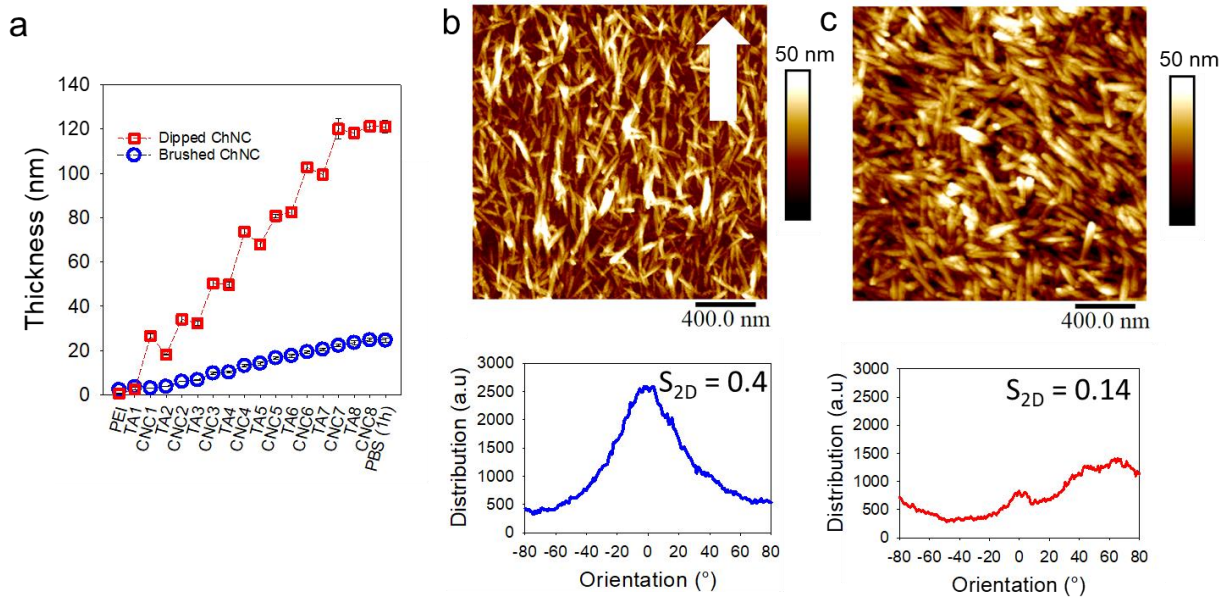

Figure 2. Thickness and surface characterization of ChNC LbL films. (a) Evolution of the thickness as a function of the last deposited layer followed by contact with PBS. For sake of clarity, the incremental thickness (< 1 nm) of Fe^{3+} is not reported. The standard deviations are not visible due to the scale of the y-axis. Typical atomic force microscopy (AFM) topography images and their orientation distribution graphs, with the order parameter S_{2D} of **(b)** the brushed and **(c)** the dipped ChNC films, *i.e.* PEI-(TA/Fe^{3+}/ChNC/Fe^{3+})$_7$-TA/Fe^{3+}/ChNC. The brushing direction, visible on the video camera, is indicated by the white arrow.

The low magnification light microscopy and scanning electron microscopy (SEM) images of the brushed ChNC films show the presence of parallel patterns in the brushing direction (Supporting Information, Figure S5). In contrast, the dipped films appeared homogeneous with a dense coverage of the surface by ChNCs. The ChNC films were then imaged by atomic force microscopy (AFM) in the dry state to characterize their topography (Figure 2b-c). In contrast to the dipped films, the ChNCs

of the brushed ChNC/TA films were preferentially oriented along the brushing direction. To characterize their degree of orientation, the AFM topography images were analyzed using OrientationJ (Supporting Information Figure S6). The orientation distribution curve of the brushed ChNC/TA films shows a maximum at 0° (*i.e.* along the brushing direction) and nanocrystals oriented between -40° and +40° (Figure 2b). In contrast, the dipped films result in randomly distributed nanocrystals with an almost flat distribution curve (Figure 2c). The shearing effect of the brushing allowed an efficient orientation of the ChNC with the order of orientation "S_{2D}" (values ranging from 0 to 1, random orientation when $S_{2D} = 0$, perfect alignment when $S_{2D} = 1$) at 0.40 and 0.14 for the brushed and dipped films, respectively.[14] The cross-section of the AFM topography images shows peaks of 20-30 and 15-25 nm in height for the brushed and dipped films, respectively (Figure 2d). The thickness of the brushed ChNC films was verified by AFM imaging of the cross-section of a scratched film. The thickness of the 8 brushed quadrilayers was 23.1 ± 2.7 nm (Supporting Information Figure S7) in agreement with the value obtained by ellipsometry. TA, TA/Fe^{3+}, and ChNC/Fe^{3+}-terminated brushed films showed similar topography features with S_{2D} values of 0.57, 0.34, and 0.44, respectively (Supporting Information Figure S8). In the following, the brushed and the dipped ChNC films of the eight ChNC terminated quadrilayers, *i.e.* PEI-(TA/Fe^{3+}/ChNC/Fe^{3+})$_7$-TA/Fe^{3+}/ChNC, will be referred to as oriented and nonoriented ChNC films, respectively.

1.2. Antibacterial activity of ChNC LbL films

Bacterial adhesion is the first step before surface colonization leads to biofilm (with a polysaccharide-rich matrix), which protects bacteria from the action of antibiotics. *S. aureus* is known to cause nosocomial and device-associated infections[41] and *E. coli* is the most common cause of catheter-associated infections.[42] Therefore, the antibacterial properties of the oriented and nonoriented ChNC films were evaluated against *S. aureus* and *E. coli* by assessing bacterial adhesion at a short time (1.5 h) and proliferation during 24 h as well as biofilm formation after 48 h of *S. aureus* incubation. A Live/Dead™ assay was performed to observe bacterial growth on the surface of the films, with live bacteria stained green (SYTO®-9 stain) and damaged bacteria strained red (propidium

iodide stain, PI). Note that no reduction in bacterial growth of both species was observed in the supernatant of either ChNC film compared to uncoated glass (Supporting Information Figure S9).

1.2.1. Oriented ChNC film prevents bacterial adhesion

For both bacterial species, the confocal optical microscopy images clearly show fewer bacteria adhering to the oriented ChNC films compared to the nonoriented films and uncoated glass (Figures 3a and c). The oriented ChNC films show approximately 86% reduction in the number of live *S. aureus* (green staining) compared to uncoated glass (with $p\text{-value} \leq 0.0001$) (Figure 3a)**.** The nonoriented films present only about 43% reduction *vs* the uncoated glass (with $p\text{-value} \leq 0.01$). The viability of bacteria was evaluated by calculating the ratio of the number of permeabilized and damaged bacteria (red staining) and all bacteria (SYTO®-9 green staining + PI red staining). Approximately 46% of adherent *S. aureus* were damaged on the oriented ChNC films compared to only 26% and 16% on the nonoriented films and uncoated glass, respectively. For *E. coli*, bacterial adhesion on the oriented ChNC films was reduced by 46% compared to the uncoated glass (with $p\text{-value} \leq 0.01$), with 50% of the bacteria damaged (*vs.* 20% for uncoated glass) (Figure 3c). The nonoriented films showed similar results with a 41% reduction in live bacteria and the presence of 44% damaged bacteria. The oriented ChNC films show better prevention of bacterial adhesion than the nonoriented films for both bacterial strains. In this effect, contact-killing plays an important role since a significant fraction of bacteria observed on the surface are damaged, while no inhibition of bacterial growth is observed in the supernatant (Supplementary Information Figure S9ac).

1.2.2. Oriented ChNC film inhibits bacterial proliferation on the film surface

After 1.5 h of initial incubation followed by 24 h of incubation in fresh culture media, confocal microscopy images showed a dramatic effect of the oriented ChNC films with only a few *S. aureus* and *E. coli* bacteria on the surface, in contrast to that observed on the nonoriented films and uncoated glass (Figure 3b, d).

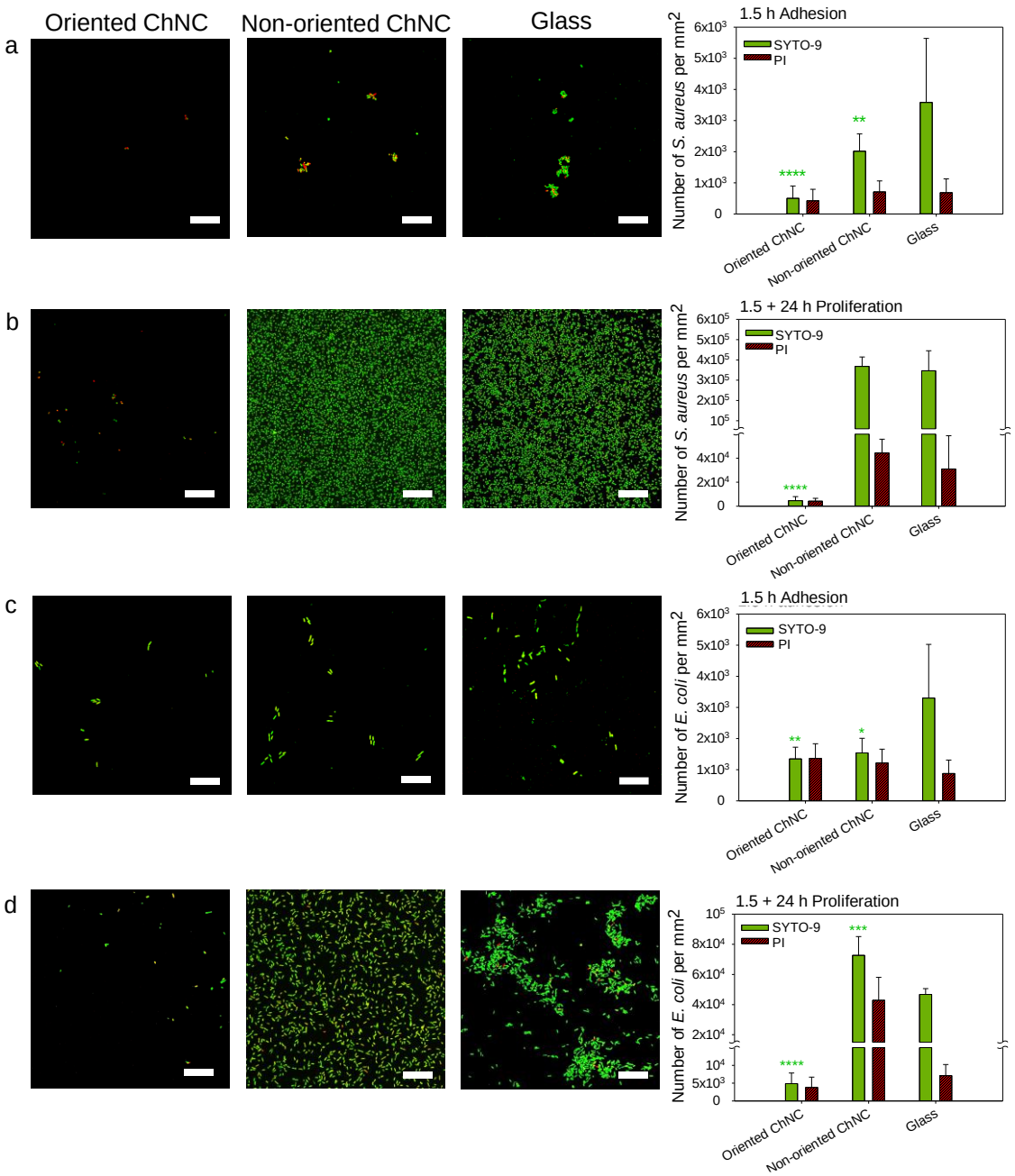

Figure 3. The contact-killing activity of the oriented ChNC films. Antibacterial properties of ChNC films determined by the Live/Dead™ assay, which stains live bacteria green (SYTO®-9) and damaged ones red (PI). Typical confocal microscopy images in combined channels (scale bar: 20 µm) and the corresponding number of bacteria adhered per mm^2 (at least 7 samples, 21 images) **(a, b)** of *S. aureus* and **(c, d)** *E. coli* after **(a, c)** 1.5 h incubation and **(b, d)** followed by 24 h proliferation at 37°C. The two-tail student t-test was calculated on the number of SYTO-9 labeled bacteria in comparison to the uncoated glass (*p≤ 0.05, **p ≤ 0.01, ***p ≤ 0.001, and ****p ≤ 0.0001). As the total number of adherent bacteria is dramatically different, the statistical test on the number of PI-labelled bacteria does not seem relevant and was not performed.

Compared to the uncoated glass, the oriented ChNC films decreased the number of live *S. aureus* (green staining) by almost 2-log (98.6%, *p-value* ≤ 0.0001) and *E. coli* by 1-log (90%, *p-value* ≤ 0.0001), with 48% and 44% damaged adherent bacteria, respectively (Figure 3b-d). The nonoriented films showed unchanged and increased proliferation of *S. aureus* and *E. coli*, respectively. The metabolic activity of *S. aureus* was assessed using the SYTO®-24/CTC Live/Dead™ assay, staining all bacteria green and respiratory active bacteria red (CTC) **(**Supplementary Information Figure S10) after 24 h of proliferation. As observed previously, few bacteria adhered to the oriented ChNC films with 48% of *S. aureus* having a respiratory activity (90% on the uncoated glass), thus confirming the detrimental effect on live bacteria (Figure 3b). Taken together, these results confirm that the reduction in colonization on the oriented ChNC is due, at least in a large part, to a surface-localized contact-killing effect rather than an antiadhesive effect, and demonstrate that it also affects the bacterial cells resulting from the proliferation of the pioneer sessile bacteria. In addition, the results show that contact-killing not only damages the cell wall but also a viable function such as respiration.

1.2.3. Oriented ChNC film prevents biofilm formation

To investigate the long-term surface activity, biofilm assays were performed with 48 h incubation of high *S. aureus* density. The SYTO®-24/CTC staining showed the presence of only a few bacteria on the oriented ChNC films in contrast to the nonoriented films and the uncoated glass (Figure 4a). The biomass (i.e. the number of cells) on the oriented ChNC films was approximately 96% lower than on the uncoated glass (with a *p-value* ≤ 0.001) (Figure 4b).

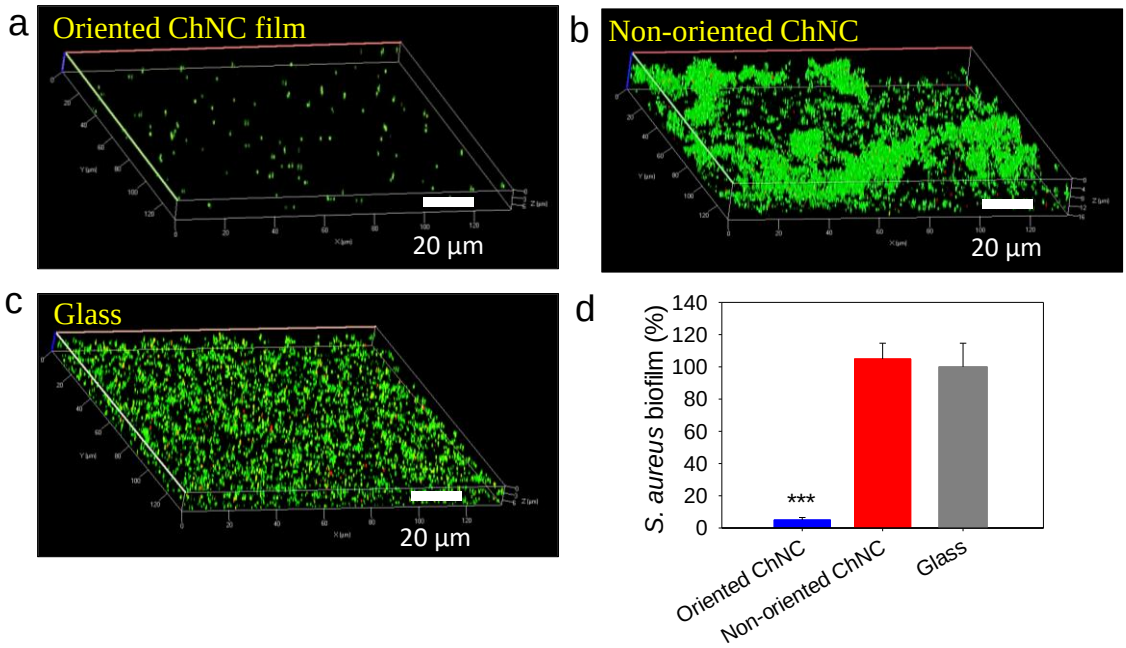

Figure 4: The antibiofilm property of ChNC LbL films. *S. aureus* biofilm on ChNC films and uncoated glass after 48 h of incubation. **(a-c)** Typical 3D confocal microscopy images after SYTO-24®/CTC staining, which stains all bacteria green (SYTO-24®) and metabolically active ones red (CTC). **(d)** Normalized biofilm quantification obtained by Safranin staining with the significance level in t-test in comparison to the uncoated glass with *** $p \leq 0.001$.

1.2.4. The crucial role of the terminating layer of ChNC-oriented films on the antibacterial activity

Knowing that they have a similar nanotopography (Supplementary Information Figure S8), the antibacterial properties of ChNC-based oriented films with different terminating layers were evaluated against *S. aureus*. Bacterial adhesion and proliferation were assessed using the SYTO®-9/PI Live/Dead™ assay on the oriented ChNC/Fe^{3+}, TA, and TA/Fe^{3+}-terminated films corresponding to (TA/Fe^{3+}/ChNC/Fe^{3+})$_8$, (TA/Fe^{3+}/ChNC/Fe^{3+})$_7$-TA, and TA/Fe^{3+}/ChNC/Fe^{3+})$_7$-TA/Fe^{3+} LbL films, respectively. The oriented ChNC/Fe^{3+}, TA, and TA/Fe^{3+} films showed higher colonization with more adherent bacteria compared to the oriented ChNC films terminated by ChNC (Figure 5a-b). The percentage of damaged bacteria after 1.5 h of culture was between 11-14 % (similar to glass at 16%). In terms of proliferation, a weaker reduction effect was obtained on the three oriented films compared to the ChNC terminated films, but with a statistically lower number of bacteria than on the

nonoriented ChNC films and uncoated glass (with *p-value* ≤ 0.0001) and 10% damaged bacteria (similar to uncoated glass) (Figure 5c-d).

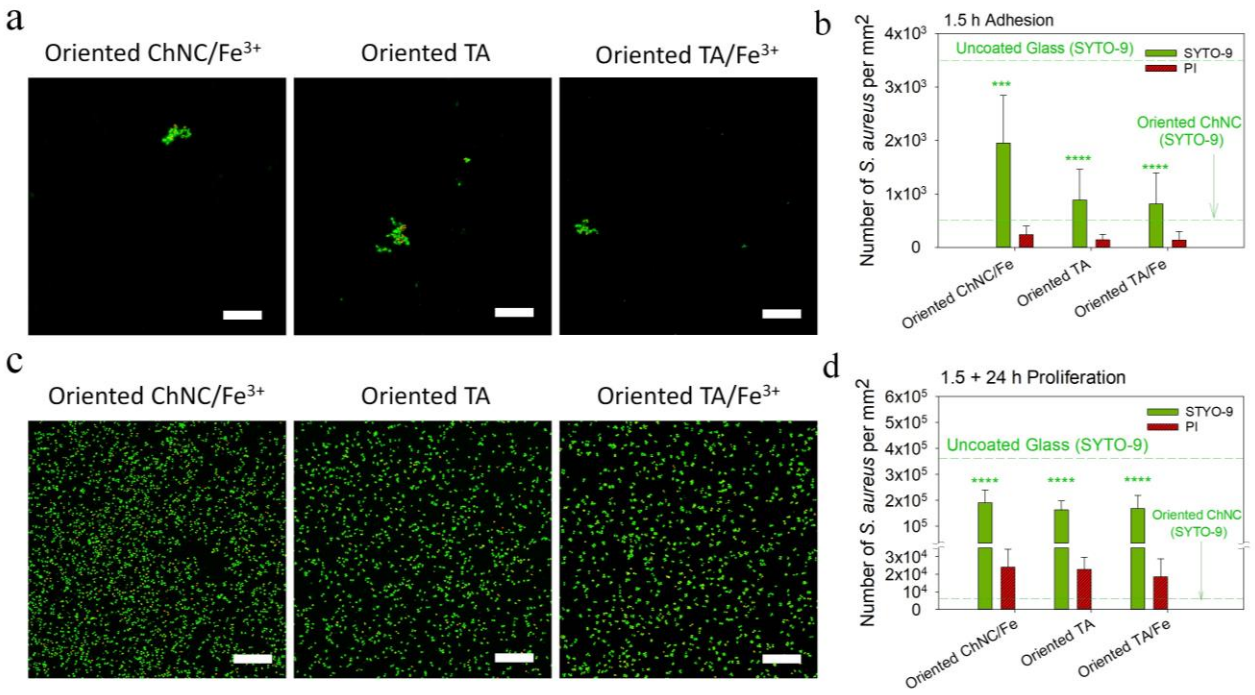

Figure 5. The crucial role of the ending layer on the antibacterial activity of the oriented ChNC films against *S. aureus*. Typical confocal microscopy images (combined green and red channels, scale bar: 20 µm) and the corresponding number of bacteria adhered per mm^2 (at least 7 samples, 21 images) for the bacterial (a, b) adhesion and (c, d) proliferation after SYTO®-9/PI Live/Dead assay of live bacteria green (SYTO®-9) and damaged ones red (PI). The values obtained in SYTO®-9 staining for the uncoated glass and the oriented ChNC films are represented by two dashed green lines. The significance level in the t-test was performed on SYTO®-9 staining in comparison to the uncoated glass *** $p \leq 0.001$ and **** $p \leq 0.0001$.

Thus, the results showed a clear effect of the ChNC terminated layer on the antibacterial properties of the oriented ChNC films. In the case of Fe^{3+}-terminated films, iron could affect the antibacterial activity as it is an essential nutrient for bacteria. On TA-terminated films, even though TA is known to be antibacterial in solution,[43] but its immobilized form is usually not.[44]

1.3. Insight into the mode of action of the oriented ChNC films

ChNC-terminated oriented films showed strong contact-killing antibacterial activity with a possible antiadhesive property against *S. aureus* and *E. coli*. Few studies have reported the antibacterial property of chitin-based films or materials. ChNC/starch blend membranes have been reported to be bacteriostatic against *L. monocytogenes* (Gram-positive) but not against *E. coli* (Gram-negative).[45] The antibacterial activity of ChNC is described as being due to its interaction with the negatively charged bacterial cell wall, altering permeability and causing membrane rupture and leakage of intracellular material, followed by cell death.[46] To gain more insight into the mechanism of action, we characterized the properties of adherent *S. aureus* on ChNC films and the surface properties of the films in comparison to the glass substrate.

1.3.1. Membrane integrity and mechanical properties of adherent S. aureus

The membrane integrity of adherent *S. aureus* was assessed by SEM after their proliferation on the different ChNC-based films compared to uncoated glass. The few adherent bacteria found on oriented ChNC films had severely damaged cell wall membranes (Figure 6a). More bacteria were present on the nonoriented ChNC films, oriented ChNC/Fe^{3+}, TA/Fe^{3+}, and TA-terminated films as well as uncoated glass with less damaged bacteria (Supplementary Information Figure S11**).** Interestingly, the cell-wall thickness of the adherent *S. aureus* was significantly higher on the oriented ChNC films (86 ± 17 nm, p values < 0.0001) than on glass (38 ± 5 nm) and about 60 nm on the nonoriented ChNC films and the other oriented films (Figure 6b). This increase in cell-wall thickness can probably explain the higher stiffness values of bacteria in contact with the oriented ChNC film (2.00 ± 0.05 MPa), and the other films tested, compared to those on the uncoated glass (0.80 ± 0.05 MPa) as shown in Figure 6c. Thickening of the *S. aureus* cell wall is commonly associated with antibiotic resistance.[47] This bacterial strain can reversibly switch from the wild-type to a different phenotype (small colony variants) resulting in an almost twofold increase in cell wall thickness in an attempt to survive in harsh environmental conditions, usually after a few days.[48]

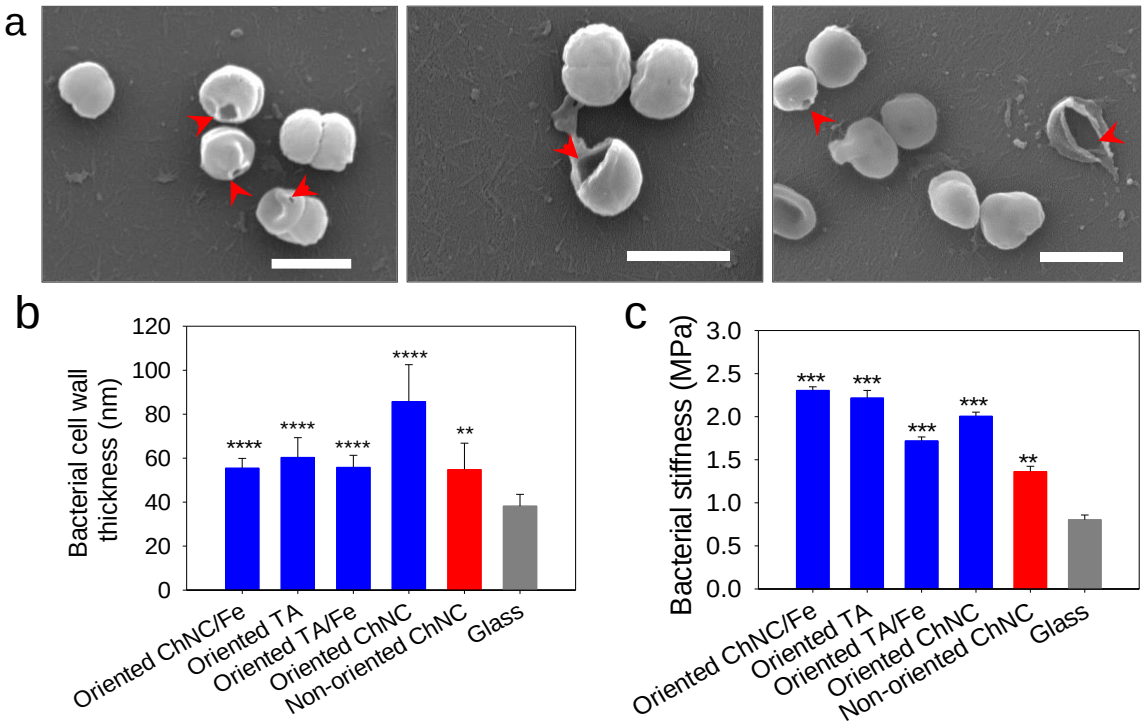

Figure 6: Characterization of adherent *S. aureus* on the ChNC-based films vs glass after 24 h proliferation. (a) Morphology, observed by SEM, on the oriented ChNC films (Scale bar: 1 µm) and **(b)** Bacterial cell wall thickness, calculated from SEM images, and **(c)** stiffness, determined by AFM nanoindentation technique, with the significance level in ANOVA test in comparison to the uncoated glass with * $p \leq 0.05$, ** $p \leq 0.05$, *** $p \leq 0.001$, and **** $p \leq 0.0001$.

Nanopillar-structured surfaces have been reported to cause stiffening of bacterial cell walls due to induced mechanical stresses superseding the cell wall elasticity, leading to membrane perforation, loss of cell contents, and ultimately cell death.[51] The increase in cell wall thickness on the oriented ChNC films may therefore be due to an adaptation and survival strategy of *S. aureus* to the harsh environment provided by the films. The increase in cell wall stiffness may be the result of this change in thickness or the direct effect of the mechanical stresses exerted on the cell membrane by the ChNC on the film surface.

1.3.2. Nanotopography characterization of ChNC-based films

Spike-like topographic features of the oriented ChNC films were observed from the three-dimensional (3D) AFM images as well as the cross-sectional profiles, where the oriented ChNC films

had more and higher peaks (20-30 up to 40 nm in height) than the nonoriented ChNC films (less than 25 nm in height) (Figure 7a and Supplementary Information Figure S8b).

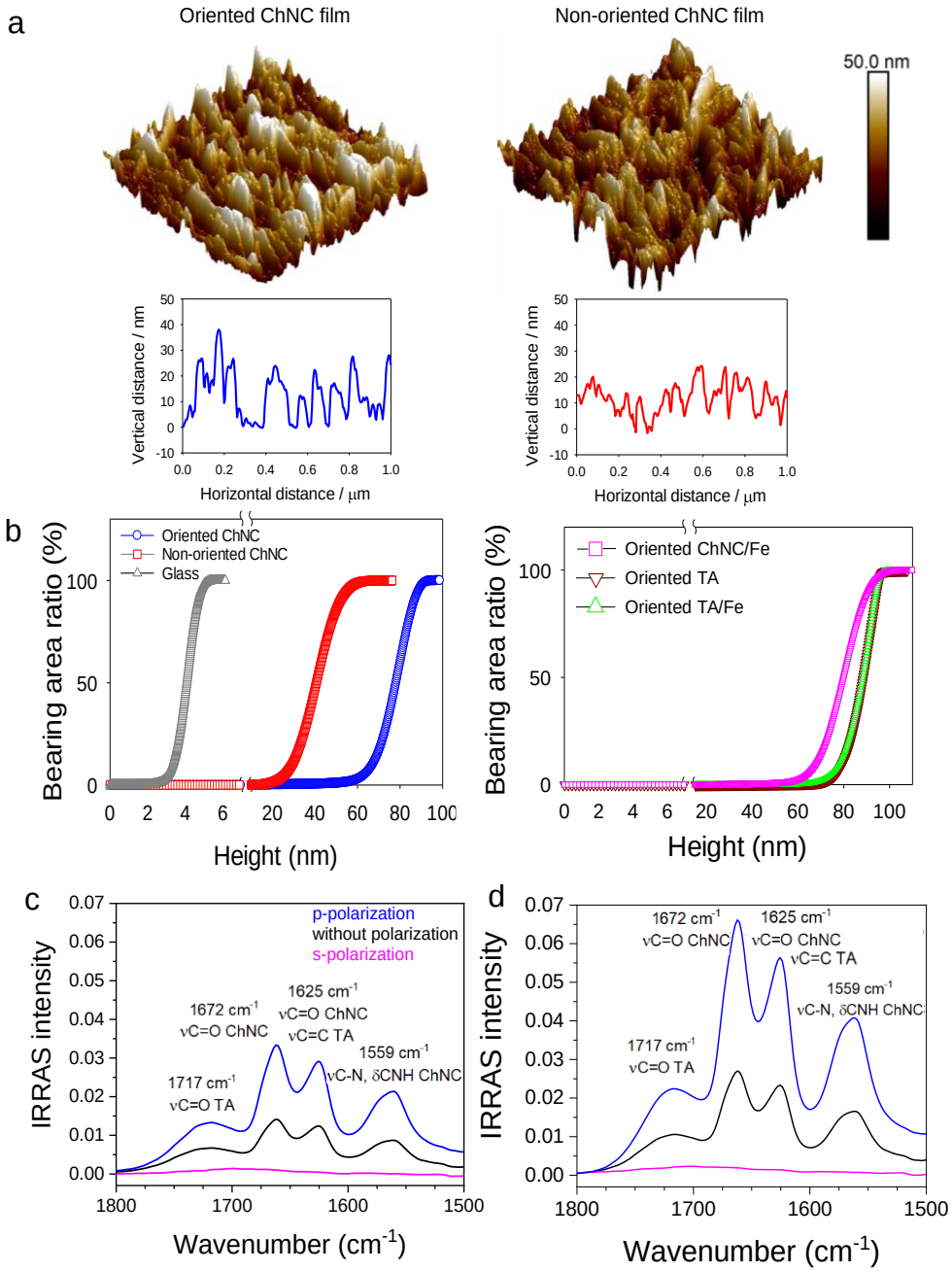

Figure 7: Nanotopography and chemical characterization of the ChNC-based films. (a) 3D AFM images (1 × 1 μm^2) of the topography of ChNC films with their respective cross-section profiles. **(b)** Bearing area ratio, calculated from AFM topography images, as a function of the height of the ChNC-based films and the uncoated glass. Infrared spectra in reflection absorption mode (IRRAS) of **(c)** the oriented and **(d)** nonoriented ChNC films.

We evaluated the difference in nanotopography between the ChNC LbL films using the bearing analysis on the AFM topography images. This method allows analyzing the distribution of the heights over a surface by plotting the percentage of the surface (*y*-axis), *i.e*. the bearing area ratio, which is above the selected height (*x*-axis) (Figure 7b). [52] A sharp increase in the bearing area ratio was observed at 60 nm for all the oriented films regardless of the final layer, 20 nm for the nonoriented CNC films, and 2 nm for uncoated glass. The increase in bearing area ratio at higher values of heights is related to a rougher topography. Infrared reflection absorption spectra (IRRAS) were recorded on the oriented and nonoriented ChNC films, deposited on a gold substrate, to have information on the molecular orientation of ChNC (Figure 7c-d and Supplementary Information Figure S12). The bands' wavenumbers and assignments are gathered in Supplementary Information Table S1. The band assignments were found in the literature[53, 54] and the spectra of pure ChNC and TA compounds (Supplementary Information Figure S12). The spectral features show the presence of ChNC and TA in both films with different overall intensities. In the 1800-1480 cm^{-1} region, the spectra are dominated by band absorptions at 1717 cm^{-1} from TA (C=O, esters of gallic acid units), 1662 cm^{-1} from ChNC (C=O, amide I band), 1625 cm^{-1} from ChNC (C=O, acetyl group) and TA (C=C aromatic skeletal rings), and 1559 cm^{-1} from ChNC (amide II band) (Figure 7c-d). The high reflectivity of p-polarized light on metals allows the measurement of only vibrations with a component of the transition dipole moment oriented perpendicular to the surface.[55] Considering the fingerprint region (1900-700 cm^{-1}) without polarized or with a p-polarized IR beam, the calculated integrated intensities were about 2 times higher for the nonoriented ChNC films compared to the oriented ones. With the film thickness measured to be 121.3 ± 2.8 nm for the nonoriented films and 24.8 ± 0.8 nm for the oriented ones (Figure 1a), the integrated intensity ratio should be about 5 times higher instead of 2. Thus, despite a lower amount of ChNC deposited, the oriented films have more vibrational modes oriented perpendicular to the surface plane than the nonoriented films, showing a higher spatial organization in this direction. This confirms the spike-like topography of the oriented ChNC films.

1.3.3. Surface charge plays a critical role in bacterial death

The nature of the terminal layer plays a crucial role as the most effective antibacterial activity is obtained by terminating with the ChNC layer. Chemical force microscopy (CFM) was used to characterize the surface charge density of the different studied films.[56] The chemical interaction between the tip and the surface was measured by converting the deflection of the AFM cantilever during the AFM tip withdrawal into adhesion force.[52, 57] The positive surface charge of the films was characterized using a phosphate-functionalized AFM probe, to mimic the bacterial cell membranes, in PBS at pH 7.4. Since the radius of the contact area of *S. aureus* on flat surfaces is in the range of several hundred nanometers,[58] the mapping of the adhesion force was determined on the 5×5 μm^2 surface area of the samples. A statistically higher adhesion force, *i.e.* interactions between the phosphate tip and the surface, was observed for the non-oriented and oriented ChNC-based films independently of the final layer compared to the uncoated glass (Figure 8a, Supplementary Information Table S2). With a median value of 0.35 nN (p-value < 0.001), a higher density of positive charges and adhesion force were observed on the oriented ChNC films compared to the nonoriented films (Figure 8 and Supplementary Information Table S2). This result is probably related to the rougher topography of the oriented ChNC films, resulting in the availability of a higher amount of surface charges of the deposited ChNC compared to the nonoriented ChNC films. The density of charges on ChNC/Fe^{3+}, TA/Fe^{3+}, and TA-terminated films was either similar to or higher than the ChNC-terminated film with statistically similar adhesion force (Figure 8b). This could be explained by electrostatic interactions of Fe^{3+} and hydrogen bonding interactions of TA with the phosphate-functionalized tip, respectively.[59]

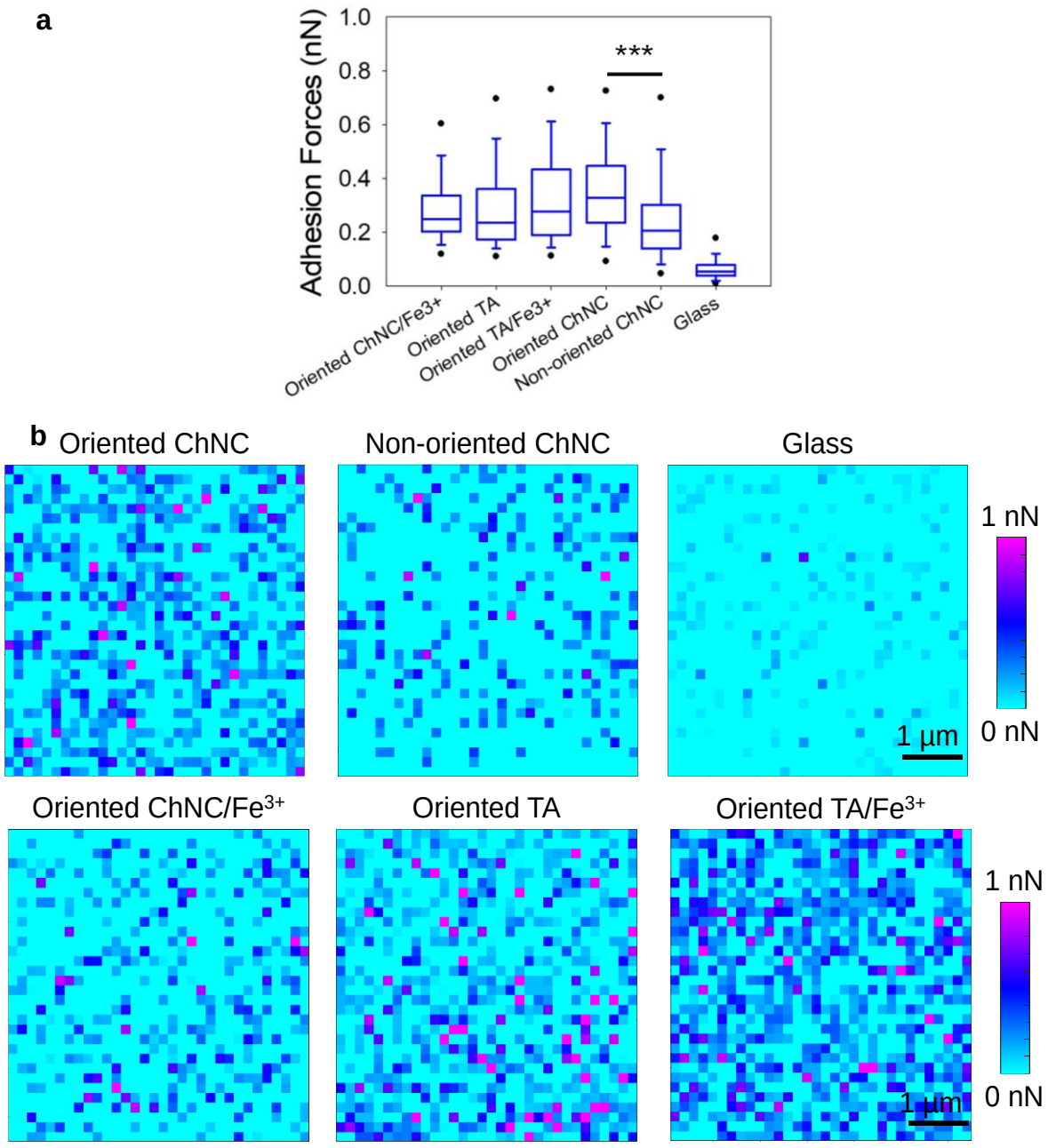

Figure 8: Surface charge density of ChNC-based films. Adhesion forces, measured by chemical force microscopy (CFM) using a phosphonate-functionalized AFM tip, **(a)** box-chart showing the median (line), the 5% and 95% quartiles, with the significance level in ANOVA test in comparison to the uncoated glass with *** $p \leq 0.001$ for all films and **(b)** mapping over a 5×5 µm^2 area of the surface of different films where each pixel represents the adhesion force measured by the functionalized AFM tip as it retracts from the sample surface.

1.4.4 Mode of action of the oriented ChNC films

The bactericidal effect of nanostructured surfaces, consisting of metals, organic/inorganic materials, or synthetic polymers, is usually associated with the mechanical rupture of cells, independent of the surface chemistry and possible antiadhesive properties resulting from the nanoscale topography. Two mechanisms of bacterial cell rupture on nanostructured surfaces have been described in the literature: (i) compression of the bacteria on the nanopillars under sedimentation forces, leading to puncture or rupture of the bacterial cell wall[3] and (ii) a combination of strong adhesion between the cells and the nanopillars, and a shear force exerted on the adherent bacteria as they move away from their initial adhesion site. The shear force can be due to their motility or to the hydrodynamic or thermodynamic motion of the fluid environment. Under this stress, the cell wall of the highly adherent bacteria is thought to rupture. Recently, Elena P. Ivanova and coworkers demonstrated that the mechanical injury caused is not sufficient to kill the bacteria immediately, due to the survival of the inner plasma membrane, but leads to apoptosis-like death. This work also showed that the mechano-bactericidal actions have sustained physiological effects on the bacterium, due to the self-accumulation of reactive oxygen species.[60] As an example of the first mechanism, it has been reported that cicada wings have bactericidal activity only against Gram-negative bacteria due to a specific nanopillar topography responsible for the stretching and further rupture of the adherent bacterial wall between two adjacent nanopillars.[4, 5] It can be hypothesized that the contact-killing property of the oriented ChNC films is due to similar mechanisms, thanks to the spike-like nanotopography (20-30 up to 40 nm in height). This leads to a thickening of the bacterial cell wall to resist the rupture and also increases its rigidity for all the ChNC-based oriented films that have the same nanotopography features. The second mechanism may also play an important role in the ChNC-terminated oriented films, which has been proposed to occur on strongly adhesive nanostructured,[4, 61] or strongly positive surfaces.[62] The higher charge of the ChNC-oriented films leads to stronger and multiple interactions between the positively charged spikes and the negatively charged bacterial cell wall. Thus, the ChNC-terminated oriented films are likely to cause more stretching and further rupture of the cell wall when bacteria

are forced to move away from their attachment location compared to the other films. As a result, they have the strongest contact-killing property (with between 44-50% damaged *S. aureus* and *E. coli*), whereas the other oriented films have only between 11-14% damaged *S. aureus*. Finally, the steeper spike-like character and the higher positive charge of the oriented ChNC film are both likely to cause the antibacterial property of this surface by leading to the cell wall puncture induced either by the compression of bacterial cells on the spikes and/or by a shear force applied to highly electrostatically adherent cells (Figure 9).

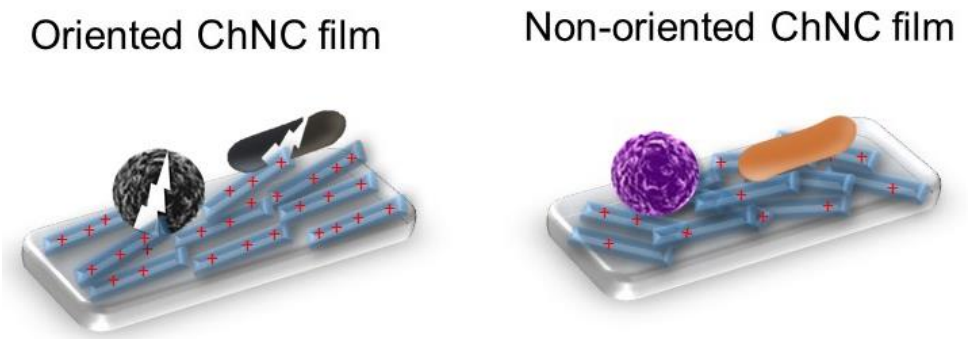

Figure 9: Contact-killing mechanism of the oriented ChNC film. A schematic representation of the nanotopographical orientation of ChNC in spike-like features with a high surface density of positive charges of the oriented ChNC films, explaining its antibacterial activity by contact-killing against *S. aureus* and *E. coli* and the nonoriented ChNC films, with a smoother surface and less surface density of positive charge.

1.4. Conclusions

Inspired by chitin-based butterfly wings and iron-rich crustacean exoskeletons, we developed the first ChNC-based LbL films with contact-killing properties against both *S. aureus* and *E. coli* as well as antibiofilm properties. The antibacterial property of the films is related to spike-like nanotopographies with a high density of positive charge on the surface, which are obtained by orienting ChNC by the brushing method in combination with TA and Fe^{3+} as partners. The puncture and associated damage of the adherent bacteria on the oriented ChNC films are likely caused by (i) the compression of the bacterial cell wall on the spike-like structures and/or (ii) the stress exerted on the adherent bacteria

cell wall by the positively charged spikes under the shear force due to bacterial motility or movement of the liquid environment. This hypothesis is supported by the morphology and mechanical properties of bacterial cell walls. The fully bio-based nature of ChNC-based nanocoatings and their brush-based fabrication method make them a suitable and affordable candidate as a sustainable antibacterial film for (bio)materials.

CRediT authorship contribution statement

Muhammad Haseeb Iqbal: Methodology, Investigation, Validation, Formal Analysis, Funding acquisition, Writing original draft. **Fabienne Quilès**: Methodology, Investigation, Formal Analysis, Writing - review & editing. **Emeline Pradel**: Investigation. **Sarah Benmalek-Kehili**: Investigation. **Christine Lancelon-Pin:** Investigation. **Laurent Heux**: Investigation, Resources. **Florent Meyer**: Conceptualization, Resources, Supervision, **Lydie Ploux**: Supervision, Resources, Writing - review & editing, Supervision. **Gregory Francius**: Methodology, Investigation, Resources, Formal Analysis, Writing - review & editing. **Fouzia Boulmedais**: Conceptualization, Supervision, Resources, Funding acquisition, Writing - review & editing, Project administration.

Declaration of Competing Interest

The authors declare that they have no known competing financial interests or personal relationships that could have appeared to influence the work reported in this paper.

Acknowledgments

The authors thank the CarMAc of ICS https://www.ics-cnrs.unistra.fr/plateforme-carmac.html, the Spectroscopy and Microscopy Service Facility (SMI) of LCPME www.lcpme.ul.cnrs.fr/equipements/smi/, where the AFM and infrared experiments were performed and the NanoBio- ICMG Platform (UAR 2607, Grenoble) for granting access to the Electron Microscopy facility. M.H.I. thanks the Higher Education Commission (HEC) Pakistan for his Ph.D. scholarship. Fonds Régional de Coopération pour la Recherche of Région Grand Est ERMES project

and International Centre for Frontier Research in Chemistry (icFRC) are acknowledged for financial support.

Appendix A. Supplementary material

Supplementary data to this article can be found online at.

Data availability statement.

Data available upon request.

References

[1] E. Fadeeva, V.K. Truong, M. Stiesch, B.N. Chichkov, R.J. Crawford, J. Wang, E.P. Ivanova, Bacterial Retention on Superhydrophobic Titanium Surfaces Fabricated by Femtosecond Laser Ablation, Langmuir 27 (2011) 3012-3019.

[2] L. Chen, X.Y. Song, F. Xing, Y.A. Wang, Y.Z. Wang, Z.Y. He, L. Sun, A Review on Antimicrobial Coatings for Biomaterial Implants and Medical Devices, Journal of Biomedical Nanotechnology 16 (2020) 789-809.

[3] E.P. Ivanova, J. Hasan, H.K. Webb, V.K. Truong, G.S. Watson, J.A. Watson, V.A. Baulin, S. Pogodin, J.Y. Wang, M.J. Tobin, C. Löbbe, R.J. Crawford, Natural Bactericidal Surfaces: Mechanical Rupture of Pseudomonas aeruginosa Cells by Cicada Wings, Small 8 (2012) 2489-2494.

[4] D.P. Linklater, V.A. Baulin, S. Juodkazis, R.J. Crawford, P. Stoodley, E.P. Ivanova, Mechano-bactericidal actions of nanostructured surfaces, Nature Reviews Microbiology 19 (2021) 8-22.

[5] A. Tripathy, P. Sen, B. Su, W.H. Briscoe, Natural and bioinspired nanostructured bactericidal surfaces, Advances in colloid and interface science 248 (2017) 85-104.

[6] O. Etienne, C. Picart, C. Taddei, Y. Haikel, J.L. Dimarcq, P. Schaaf, J.C. Voegel, J.A. Ogier, C. Egles, Multilayer polyelectrolyte films functionalized by insertion of defensin: a new approach to protection of implants from bacterial colonization, Antimicrob. Agents Chemother. 48 (2004) 3662-9.

[7] G. Cado, R. Aslam, L. Séon, T. Garnier, R. Fabre, A. Parat, A. Chassepot, J.-C. Voegel, B. Senger, F. Schneider, Y. Frère, L. Jierry, P. Schaaf, H. Kerdjoudj, M.-H. Metz-Boutigue, F. Boulmedais, Self-defensive biomaterial coating against bacteria and yeasts: polysaccharide multilayer film with embedded antimicrobial peptide, Adv. Funct. Mat. 23 (2013) 4801–4809.

[8] L. Chen, X. Song, F. Xing, Y. Wang, Y. Wang, Z. He, L. Sun, A Review on Antimicrobial Coatings for Biomaterial Implants and Medical Devices, Journal of Biomedical Nanotechnology 16 (2020) 789-809.

[9] G. Decher, Fuzzy Nanoassemblies: Toward Layered Polymeric Multicomposites, Science 277 (1997) 1232-1237.
[10] C. Jiang, S. Markutsya, V.V. Tsukruk, Collective and individual plasmon resonances in nanoparticle films obtained by spin-assisted layer-by-layer assembly, Langmuir 20 (2004) 882-890.
[11] J.B. Schlenoff, S.T. Dubas, T. Farhat, Sprayed Polyelectrolyte Multilayers, Langmuir 16 (2000) 9968-9969.
[12] L. Séon, P. Lavalle, P. Schaaf, F. Boulmedais, Polyelectrolyte Multilayers: A Versatile Tool for Preparing Antimicrobial Coatings, Langmuir 31 (2015) 12856-12872.
[13] K. Park, D. Choi, J. Hong, Nanostructured Polymer Thin Films Fabricated with Brush-based Layer-by-Layer Self-assembly for Site-selective Construction and Drug release, Sci. Rep. 8 (2018) 3365.
[14] X. Zhao, C. Zhou, Y. Lvov, M. Liu, Clay Nanotubes Aligned with Shear Forces for Mesenchymal Stem Cell Patterning, Small 15 (2019) 1900357.
[15] S.-M. Chen, H.-L. Gao, Y.-B. Zhu, H.-B. Yao, L.-B. Mao, Q.-Y. Song, J. Xia, Z. Pan, Z. He, H.-A. Wu, S.-H. Yu, Biomimetic twisted plywood structural materials, Natl. Sci. Rev. 5 (2018) 703-714.
[16] M.H. Iqbal, F.J.R. Revana, E. Pradel, V. Gribova, K. Mamchaoui, C. Coirault, F. Meyer, F. Boulmedais, Brush-Induced Orientation of Collagen Fibers in Layer-by-Layer Nanofilms: A Simple Method for the Development of Human Muscle Fibers, ACS Nano 16 (2022) 20034-20043.
[17] J.F. Revol, R.H. Marchessault, In vitro chiral nematic ordering of chitin crystallites, Int. J. Biol. Macromol. 15 (1993) 329-335.
[18] Y. Tian, K. Liang, X. Wang, Y. Ji, Fabrication of Nanocomposite Bioelastomer Porous Scaffold Based on Chitin Nanocrystal Supported Emulsion-Freeze-Casting, ACS Sustain. Chem. Eng. 5 (2017) 3305-3313.
[19] B. Duan, X. Zheng, Z. Xia, X. Fan, L. Guo, J. Liu, Y. Wang, Q. Ye, L. Zhang, Highly Biocompatible Nanofibrous Microspheres Self-Assembled from Chitin in NaOH/Urea Aqueous Solution as Cell Carriers, Angew. Chem., Int. Ed. 54 (2015) 5152-5156.
[20] M.Y. Boltoeva, I. Dozov, P. Davidson, K. Antonova, L. Cardoso, B. Alonso, E. Belamie, Electric-Field Alignment of Chitin Nanorod–Siloxane Oligomer Reactive Suspensions, Langmuir 29 (2013) 8208-8212.
[21] T.T. Nge, N. Hori, A. Takemura, H. Ono, T. Kimura, Synthesis and orientation study of a magnetically aligned liquid-crystalline chitin/poly(acrylic acid) composite, J. Polym. Sci., Part B: Polym. Phys. 41 (2003) 711-714.

[22] A. Mendoza-Galvan, E. Muñoz, K. Järrendahl, H. Arwin, Birefringence of nanocrystalline chitin films studied by Mueller-matrix spectroscopic ellipsometry, Opt. Mater. Express 6 (2016) 671.
[23] J.G. Torres-Rendon, F.H. Schacher, S. Ifuku, A. Walther, Mechanical Performance of Macrofibers of Cellulose and Chitin Nanofibrils Aligned by Wet-Stretching: A Critical Comparison, Biomacromolecules 15 (2014) 2709-2717.
[24] N.R. Sudarshan, D.G. Hoover, D. Knorr, Antibacterial action of chitosan, Food Biotechnol. 6 (1992) 257-272.
[25] A.M. Salaberria, S.C.M. Fernandes, R.H. Diaz, J. Labidi, Processing of α-chitin nanofibers by dynamic high pressure homogenization: Characterization and antifungal activity against A. niger, Carbohydr. Polym. 116 (2015) 286-291.
[26] B. Ma, A. Qin, X. Li, X. Zhao, C. He, Structure and properties of chitin whisker reinforced chitosan membranes, Int. J. Biol. Macromol. 64 (2014) 341-346.
[27] Y. Zhang, J. Jiang, L. Liu, K. Zheng, S. Yu, Y. Fan, Preparation, assessment, and comparison of α-chitin nano-fiber films with different surface charges, Nanoscale Res. Lett. 10 (2015) 226.
[28] D. Solairaj, P. Rameshthangam, P. Muthukumaran, J. Wilson, Studies on electrochemical glucose sensing, antimicrobial activity and cytotoxicity of fabricated copper nanoparticle immobilized chitin nanostructure, Int. J. Biol. Macromol. 101 (2017) 668-679.
[29] A. Villares, C. Moreau, I. Capron, B. Cathala, Chitin Nanocrystal-Xyloglucan Multilayer Thin Films, Biomacromolecules 15 (2014) 188-194.
[30] Z.-D. Qi, T. Saito, Y. Fan, A. Isogai, Multifunctional Coating Films by Layer-by-Layer Deposition of Cellulose and Chitin Nanofibrils, Biomacromolecules 13 (2012) 553-558.
[31] K. Manabe, C. Tanaka, Y. Moriyama, M. Tenjimbayashi, C. Nakamura, Y. Tokura, T. Matsubayashi, K.-H. Kyung, S. Shiratori, Chitin Nanofibers Extracted from Crab Shells in Broadband Visible Antireflection Coatings with Controlling Layer-by-Layer Deposition and the Application for Durable Antifog Surfaces, ACS Appl. Mater. Interfaces 8 (2016) 31951-31958.
[32] T. Taniguchi, K.-H. Kyung, S. Shiratori, Layer-by-layer self-assembled thin films of chitin fibers and heparin with anti-thrombus characteristics, RSC Advances 5 (2015) 107488-107496.
[33] A. Elbaz, J. Lu, B. Gao, F. Zheng, Z. Mu, Y. Zhao, Z. Gu, Chitin-Based Anisotropic Nanostructures of Butterfly Wings for Regulating Cells Orientation, Polymers 9 (2017) 386.
[34] L.M. Gordon, D. Joester, Nanoscale chemical tomography of buried organic–inorganic interfaces in the chiton tooth, Nature 469 (2011) 194-197.
[35] W. Wang, Q. Meng, Q. Li, J. Liu, M. Zhou, Z. Jin, K. Zhao, Chitosan Derivatives and Their Application in Biomedicine, Int. J. Mol. Sci. 21 (2020) 487.

[36] A. Shukla, J.C. Fang, S. Puranam, F.R. Jensen, P.T. Hammond, Hemostatic Multilayer Coatings, Adv Mater 24 (2012) 492-496.
[37] H. Ejima, J.J. Richardson, K. Liang, J.P. Best, M.P. van Koeverden, G.K. Such, J. Cui, F. Caruso, One-Step Assembly of Coordination Complexes for Versatile Film and Particle Engineering, Science 341 (2013) 154-157.
[38] J. Huang, Y.X. Cheng, Y. Wu, X.W. Shi, Y.M. Du, H.B. Deng, Chitosan/tannic acid bilayers layer-by-layer deposited cellulose nanofibrous mats for antibacterial application, International Journal of Biological Macromolecules 139 (2019) 191-198.
[39] J.M. Nieto, C. Penichecovas, J. Delbosque, Preparation and Characterization of a Chitosan-Fe(Iii) Complex, Carbohydrate Polymers 18 (1992) 221-224.
[40] E.D. Cranston, D.G. Gray, Morphological and Optical Characterization of Polyelectrolyte Multilayers Incorporating Nanocrystalline Cellulose, Biomacromolecules 7 (2006) 2522-2530.
[41] A.G. Jensen, F. Espersen, P. Skinhøj, V.T. Rosdahl, N. Frimodt-Møller, Increasing frequency of vertebral osteomyelitis following Staphylococcus aureus bacteraemia in Denmark 1980–1990, J. Infect. 34 (1997) 113-118.
[42] S.M. Jacobsen, D.J. Stickler, H.L.T. Mobley, M.E. Shirtliff, Complicated catheter-associated urinary tract infections due to Escherichia coli and Proteus mirabilis, Clin. Microbiol. Rev. 21 (2008) 26-59.
[43] D.E. Payne, N.R. Martin, K.R. Parzych, A.H. Rickard, A. Underwood, B.R. Boles, Tannic acid inhibits Staphylococcus aureus surface colonization in an IsaA-dependent manner, Infect. Immun. 81 (2013) 496-504.
[44] M.H. Iqbal, A. Schroder, H. Kerdjoudj, C. Njel, B. Senger, V. Ball, F. Meyer, F. Boulmedais, Effect of the Buffer on the Buildup and Stability of Tannic Acid/Collagen Multilayer Films Applied as Antibacterial Coatings, ACS Appl. Mater. Interfaces 12 (2020) 22601-22612.
[45] Y. Qin, S. Zhang, J. Yu, J. Yang, L. Xiong, Q. Sun, Effects of chitin nano-whiskers on the antibacterial and physicochemical properties of maize starch films, Carbohydr. Polym. 147 (2016) 372-378.
[46] A. Nagy, A. Harrison, S. Sabbani, R.S. Munson, Jr., P.K. Dutta, W.J. Waldman, Silver nanoparticles embedded in zeolite membranes: release of silver ions and mechanism of antibacterial action, Int. J. Nanomed. 6 (2011) 1833-52.
[47] L. Cui, X.X. Ma, K. Sato, K. Okuma, F.C. Tenover, E.M. Mamizuka, C.G. Gemmell, M.N. Kim, M.C. Ploy, N. El Solh, V. Ferraz, K. Hiramatsu, Cell wall thickening is a common feature of vancomycin resistance in Staphylococcus aureus, J Clin Microbiol 41 (2003) 5-14.

[48] G. Loss, P.M. Simões, F. Valour, M.F. Cortês, L. Gonzaga, M. Bergot, S. Trouillet-Assant, J. Josse, A. Diot, E. Ricci, A.T. Vasconcelos, F. Laurent, Staphylococcus aureus Small Colony Variants (SCVs): News From a Chronic Prosthetic Joint Infection, Front. Cell. Infect. Microbiol. 9 (2019) 363.
[49] L. Rizzello, B. Sorce, S. Sabella, G. Vecchio, A. Galeone, V. Brunetti, R. Cingolani, P.P. Pompa, Impact of Nanoscale Topography on Genomics and Proteomics of Adherent Bacteria, ACS Nano 5 (2011) 1865-1876.
[50] M.S. Bojer, K. Wacnik, P. Kjelgaard, C. Gallay, A.L. Bottomley, M.T. Cohn, G. Lindahl, D. Frees, J.W. Veening, S.J. Foster, H. Ingmer, SosA inhibits cell division in Staphylococcus aureus in response to DNA damage, Mol Microbiol 112 (2019) 1116-1130.
[51] Y. Deng, M. Sun, J.W. Shaevitz, Direct measurement of cell wall stress stiffening and turgor pressure in live bacterial cells, Phys. Rev. Lett. 107 (2011) 158101.
[52] N.C. Santos, F.A. Carvalho, Atomic Force Microscopy, Springer2019.
[53] L. Falcao, M.E.M. Araujo, Application of ATR-FTIR spectroscopy to the analysis of tannins in historic leathers: The case study of the upholstery from the 19th century Portuguese Royal Train, Vib Spectrosc 74 (2014) 98-103.
[54] F.G. Pearson, R.H. Marchessault, C.Y. Liang, Infrared spectra of crystalline polysaccharides. V. Chitin, J. Polym. Sci. 43 (1960) 101-116.
[55] D. Guo, X. Chen, K. Cai, P. Deng, R. Zong, Analyzing the Molecular Orientation of Ultrathin Organic Films by Polarized Transmission and Grazing Incidence Reflection Absorption IR Spectroscopy, Materials Focus 2 (2013) 231-238.
[56] X. Mi, E.K. Bromley, P.U. Joshi, F. Long, C.L. Heldt, Virus Isoelectric Point Determination Using Single-Particle Chemical Force Microscopy, Langmuir 36 (2020) 370-378.
[57] J. Kámán, Young's Modulus and Energy Dissipation Determination Methods by AFM, with Particular Reference to a Chalcogenide Thin Film, Period. polytech. Electr. eng. comput. sci. 59 (2015) 18-25.
[58] C. Spengler, N. Thewes, P. Jung, M. Bischoff, K. Jacobs, Determination of the nano-scaled contact area of staphylococcal cells, Nanoscale 9 (2017) 10084-10093.
[59] M. Shin, J.H. Ryu, J.P. Park, K. Kim, J.W. Yang, H. Lee, DNA/Tannic Acid Hybrid Gel Exhibiting Biodegradability, Extensibility, Tissue Adhesiveness, and Hemostatic Ability, Adv. Funct. Mater. 25 (2015) 1270-1278.
[60] S. Zhao, Z. Li, D.P. Linklater, L. Han, P. Jin, L. Wen, C. Chen, D. Xing, N. Ren, K. Sun, S. Juodkazis, E.P. Ivanova, L. Jiang, Programmed Death of Injured Pseudomonas aeruginosa on Mechano-Bactericidal Surfaces, Nano Letters 22 (2022) 1129-1137.

[61] K. Nowlin, A. Boseman, A. Covell, D. LaJeunesse, Adhesion-dependent rupturing of Saccharomyces cerevisiae on biological antimicrobial nanostructured surfaces, J R Soc Interface 12 (2015) 20140999.
[62] B. Gottenbos, D.W. Grijpma, H.C. van der Mei, J. Feijen, H.J. Busscher, Antimicrobial effects of positively charged surfaces on adhering Gram-positive and Gram-negative bacteria, J Antimicrob Chemoth 48 (2001) 7-13.

Graphical abstract